Inorganic Chemistry

Article

pubs.acs.org/IC

Sc_2NiMnO_6: A Double-Perovskite with a Magnetodielectric Response Driven by Multiple Magnetic Orders

Wei Yi,[†,‡] Andrew J. Princep,[§] Yanfeng Guo,[*,§] Roger D. Johnson,[§] Dmitry Khalyavin,[∥] Pascal Manuel,[∥] Anatoliy Senyshyn,[⊥] Igor A. Presniakov,[#] Alexey V. Sobolev,[#] Yoshitaka Matsushita,[▽] Masahiko Tanaka,[▽] Alexei A. Belik,[*,†] and Andrew T. Boothroyd[§]

[†]International Center for Materials Nanoarchitectonics (WPI-MANA), National Institute for Materials Science, Tsukuba, Ibaraki 305-0044, Japan

[‡]Institute of Physics and Beijing National Laboratory for Condensed Matter Physics, Chinese Academy of Sciences, Beijing 100190, China

[§]Department of Physics, University of Oxford, Clarendon Laboratory, Parks Road, Oxford, OX1 3PU, United Kingdom

[∥]ISIS Facility, Rutherford Appleton Laboratory, Chilton, Didcot, OX11 0QX, United Kingdom

[⊥]FRM-II, Technische Universität München, Garching 85747, Germany

[#]Department of Chemistry, Lomonosov Moscow State University, Leninskie Gory, 119992 Moscow, Russia

[▽]Synchrotron X-ray Station at SPring-8, NIMS, Kohto 1-1-1, Sayo-cho, Hyogo 679-5148, Japan

Supporting Information

ABSTRACT: Perovskite materials provide a large variety of interesting physical properties and applications. Here, we report on unique properties of a fully ordered magnetodielectric double-perovskite, Sc_2NiMnO_6 (space group $P2_1/n$, a = 4.99860 Å, b = 5.35281 Å, c = 7.34496 Å, and β = 90.7915°), exhibiting sequential magnetic transitions at T_1 = 35 K and T_2 = 17 K. The transition at T_1 corresponds to a single-$\mathbf{k}$ antiferromagnetic phase with propagation vector $\mathbf{k}_1$ = (1/2, 0, 1/2), while the second transition at T_2 corresponds to a 2-$\mathbf{k}$ magnetic structure with propagation vectors $\mathbf{k}_1$ = (1/2, 0, 1/2) and $\mathbf{k}_2$ = (0, 1/2, 1/2). Symmetry analysis suggests that the two ordering wave vectors are independent, and calculations imply that $\mathbf{k}_1$ is associated with the Mn sublattice and $\mathbf{k}_2$ with the Ni sublattice, suggesting that Mn−Ni coupling is very small or absent. A magnetodielectric anomaly at T_2 likely arises from an antiferroelectric ordering that results from the exchange-striction between the two magnetic sublattices belonging to $\mathbf{k}_1$ and $\mathbf{k}_2$. The behavior of Sc_2NiMnO_6 demonstrates 3d double-perovskites with small A-site cations as a promising avenue in which to search for magnetoelectric materials.

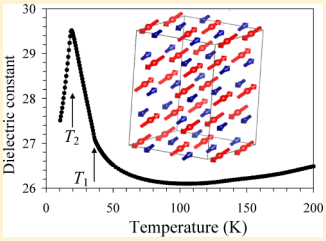

1. INTRODUCTION

Magnetodielectrics, that is, materials whose dielectric properties can be controlled by a magnetic field, or alternatively, whose magnetic ordering can produce a dielectric anomaly, have attracted scientific interest owing to their merits for both fundamental research and technological applications.[1−4] Magnetodielectric (MD) effects are typically caused by spin−lattice coupling[4] and are key to the behavior of many magnetocaloric materials and type-II multiferroics.[5,6] Non-multiferroic magnetodielectrics can be classified into two categories: frustrated magnets such as $R_2Ti_2O_7$,[7,8] and magnetic materials that show a dielectric anomaly in the vicinity of magnetic order such as Mn_3O_4,[3] $TeCuO_3$,[4] and $Dy_3Fe_5O_{12}$.[9]

The discovery and characterization of magnetodielectric materials are necessary to improve understanding of the underlying mechanisms and to optimize material properties for realistic device applications. An ideal system for such exploration is the double-perovskite structure with the formula $A_2BB'O_6$ (A is an alkaline-earth or rare-earth element; B and B′ are transition metals).[10] The B and B′ sites are able to accommodate various cations with different electronic configurations, allowing the engineering of superexchange pathways by appropriate choice of magnetic B and B′ cations. Double-perovskites thus display a wealth of magnetic properties including ferro-, ferri-, and antiferro-magnetism; multiferroicity; and the magnetocaloric effect, as well as spin-liquid and spin-glass states.[10−18]

The double-perovskite structure is susceptible to a variety of structural instabilities, and magnetoelastic coupling of the magnetic B-site ions leads to several possible magneto-structural phase transitions.[15−21] When both B and B′ are 3d metals, double-perovskites tend to be ferromagnetic (FM) insulators, and this can be understood via the Goodenough-Kanamori (G-K) rules.[22,23] Several FM double-perovskites in the Ln_2CoMnO_6 and Ln_2NiMnO_6 families (Ln = rare-earth elements) have been identified as having interesting magneto-dielectric, magnetocaloric, or multiferroic propterties.[20,24−30] The study of the mechanisms underlying these behaviors is complicated by a great sensitivity to variations in synthesis

Received: May 28, 2015

DOI: 10.1021/acs.inorgchem.5b01195
Inorg. Chem. XXXX, XXX, XXX−XXX

conditions and in particular to the degree of B/B′ cation ordering.[26,31,32] Synthesis of double-perovskite magnetodielectrics with antiferromagnetic (AFM) order would provide complementary knowledge about the relationship between magnetic structures and MD behavior, through insights into the role played by the magnetism. The recent synthesis of the AFM multiferroic In_2NiMnO_6, with a small In^{3+} cation at the A site,[33,34] where a ferroelectric polarization of 30 $\mu C/m^2$ is developed below T_N = 26 K,[35] represents a key development in this direction. The synthesis of Sc_2NiMnO_6 has been attempted in the literature;[36] however, the ordered phase has not been obtained.

In this work, we report the high-pressure synthesis, structural, magnetic, and electrical properties of the AFM double-perovskite magnetodielectric, Sc_2NiMnO_6, with the ordered structure. There is an AFM ordering transition at T_1 = 35 K to a single-**k** magnetic structure (AFM I) and a second magnetic transition at T_2 = 17 K to a 2-**k** magnetic structure (AFM II), which is accompanied by a sharp anomaly in the dielectric constant. The magnetodielectric response $[\varepsilon(H) - \varepsilon(0)]/\varepsilon(0)$ peaks at T_2 with a value of ∼2.7% for $H \sim 90$ kOe. This behavior arises from the substantial suppression of the transition temperature T_2 in response to an applied magnetic field. Neutron powder diffraction provides evidence for an unusual magnetic structure in which the Ni and Mn sublattices order independently with different wavevectors.

2. EXPERIMENTAL DETAILS

Sc_2NiMnO_6 was synthesized from a stoichiometric mixture of Sc_2O_3 (99.99%), NiO (99.9%), and MnO_2 (99.997%) by a solid-state reaction under high-pressure and high-temperature conditions. The mixture (about 0.4 g) was placed into Pt capsules and was treated at 1373−1773 K for 2 h in a press of 6 GPa in a belt-type high-pressure apparatus (Figures S1 and S2). After reaction, the samples were quenched to room temperature before the pressure was released.

Powder X-ray diffraction (XRD) data were collected at room temperature (RT) on a RIGAKU Ultima III diffractometer using Cu Kα radiation (2θ range of 10−80°, a step width of 0.02°, and a counting time of 1−10 s/step). Electron probe microanalysis (EPMA) was performed on a JEOL, JXA-8500F instrument. The surface of the pellet sample was polished on a fine (0.3 μm) alumina coated film before measurement. MnO, NiO, and Sc_2O_3 were used as standard samples for Mn, Ni, and Sc, respectively. The EPMA data supported the chemical composition of Sc:Ni:Mn = 2.02(4):0.96(2):1. The sample was then measured with synchrotron XRD at RT on a Debye−Scherrer camera at the BL15XU beamline of SPring-8.[37] The data were collected between 2° and 60° in 2θ with a step of 0.003° and an incident wavelength of 0.65297 Å. A fine powder of the sample was packed into a 0.1 mm Lindemann glass capillary which was rotated during the measurement. Obtained synchrotron XRD patterns were analyzed by the Rietveld method using the programs RIETAN-2000 and VESTA.[38,39]

Magnetic susceptibility ($\chi = M/H$) was measured on a SQUID magnetometer (Quantum Design, MPMS) between 2 and 400 K in various magnetic fields under both zero-field-cooling (ZFC) and field-cooling (FC) conditions. Isothermal magnetization measurements were performed between −50 and 50 kOe at various temperatures on the same apparatus. ^{57}Fe Mössbauer spectra were measured at 12, 25, 45, and 300 K using a conventional constant-acceleration spectrometer. The radiation source ^{57}Co/Rh was kept at RT. The obtained spectra were calibrated by α-Fe as a standard and were fitted by the Lorentzian function.

Specific heat, C_p, was measured in magnetic fields of 0, 70, and 90 kOe between 2 and 300 K on cooling by a pulse relaxation method using a commercial calorimeter (Quantum Design PPMS). Dielectric constants were measured using an Agilent E4980A LCR meter between 10 and 300 K at frequencies between 1 kHz and 1 MHz at various magnetic fields between −90 and 90 kOe.

Neutron powder diffraction (NPD) measurements were carried out on a 3.5 g powder sample at 300, 25, and 4 K on the SPODI high-resolution diffractometer at the FRM-II facility of the Technische Universität München, Germany, and also at 300, 36, 26, and 1.5 K, and in 1 K steps between 17 and 38 K on the WISH time-of-flight diffractometer at the ISIS Facility,[40] Rutherford Appleton Laboratory, United Kingdom.

3. RESULTS AND DISCUSSION

The synchrotron XRD pattern of Sc_2NiMnO_6 could only be fully indexed within monoclinic symmetry with lattice parameters a = 4.9986 Å, b = 5.3528 Å, c = 7.3450 Å, and β = 90.792° using TREOR.[41] The observed reflection conditions are consistent with the space group $P2_1/n$ (No. 14, cell choice 2) similar to other R_2NiMnO_6 (R = In, Y, and rare-earth elements). We used structural parameters of In_2NiMnO_6[33] as the starting ones in the Rietveld analysis of Sc_2NiMnO_6. The refined structural parameters, R values, selected bond lengths, and bond-valence sums (BVS)[42] are listed in Tables 1 and S1.

Table 1. Room-Temperature Structural Parameters of Sc_2NiMnO_6 from Synchrotron X-ray Powder Diffraction Data[a]

site	WP	x	y	z	B (Å^2)
Mn	2c	0.5	0	0.5	0.50(2)
Ni	2d	0.5	0	0	0.71(2)
Sc	4e	0.97474(17)	0.07530(10)	0.25372(15)	0.772(16)
O1	4e	0.3567(4)	0.9403(4)	0.2610(4)	0.81(5)
O2	4e	0.1967(5)	0.1821(5)	0.5642(3)	1.11(6)
O3	4e	0.6749(5)	0.2988(5)	0.4252(3)	1.07(6)

[a]WP: Wyckoff position. Space group is $P2_1/n$ (No. 14, cell choice 2). Z = 2, λ = 0.65297 Å. Full occupancy factors for all sites. a = 4.99860(2) Å, b = 5.35281(2) Å, c = 7.34496(2) Å, β = 90.7915(2)°, V = 196.5068(11) Å^3, and ρ = 5.062 g/cm^3. Final R values were R_{wp} = 4.08%, R_p = 2.65%, R_B = 4.81%, and R_F = 3.93%.

The experimental, calculated, and difference patterns are shown in Figure 1. The refined crystal structure is illustrated in Figure 2. The Ni and Mn ions are alternatively located in the corner-shared octahedral environments with three unique Ni−O and

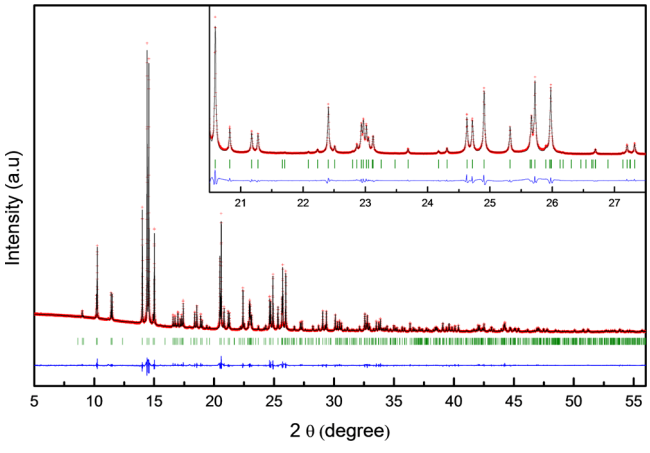

Figure 1. Observed (red), calculated (black), and difference (blue) synchrotron XRD patterns of Sc_2NiMnO_6 at RT (λ = 0.65297 Å). The small tick marks denote simulated peak positions. The inset shows enlarged view of the profiles between 20.5 and 27.5° of the 2θ range.

DOI: 10.1021/acs.inorgchem.5b01195
Inorg. Chem. XXXX, XXX, XXX−XXX

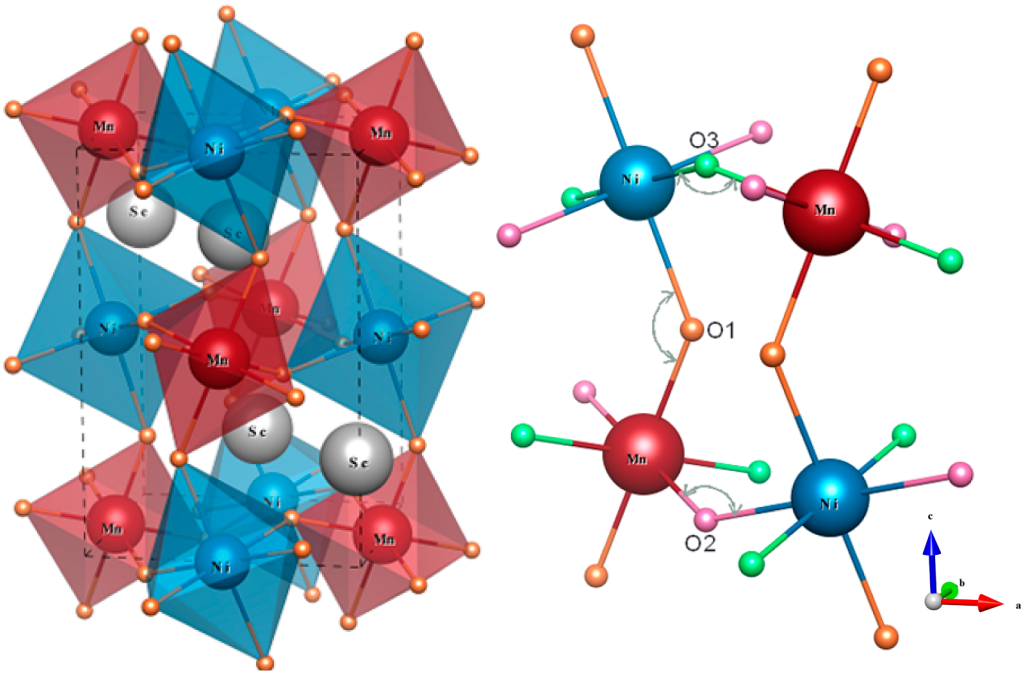

Figure 2. Crystal structure of Sc_2NiMnO_6, indicating the tilted octahedra belonging to Ni and Mn, as well as the three unique 3d−O−3d bond angles.

Mn−O distances. The BVS analysis of the metal−oxygen distances gives a valence of 4+ for Mn and 2+ for Ni. In the subsequent discussion of the NPD results, we find further evidence for the complete ordering of the Ni and Mn sites.

The lattice parameters and unit cell volume of Sc_2NiMnO_6 are all the smallest among known R_2NiMnO_6 compounds with the $P2_1/n$ space group (see Figure S3a and S3b). Moreover, Sc_2NiMnO_6 has the smallest average Ni−O−Mn bond angle of 137.4° (Figure S3d), resulting from a significant octahedral tilting of the crystal structure (pattern $a^-a^-c^+$ in the Glazer notation[43]). The magnetic ground states in R_2NiMnO_6 are often expected to be FM[30,44,45] within the framework of G-K rules because of the superexchange interaction between the half-filled e_g orbital of Ni^{2+} and the valence e_g orbital of Mn^{4+} bridged by the p orbital of O^{2-}. The FM interaction strength can be gradually reduced through the decrease of the Ni−O−Mn bond angles which reduces the hopping integral, thus monotonically decreasing the FM ordering temperature (Figure S3c)[44,45] or even stabilizing a complex noncollinear AFM ground state in multiferroic In_2NiMnO_6.[35] Y_2NiMnO_6 ($r_{VIII}(Y^{3+})$ = 1.019 Å) was predicted to be an AFM multiferroic[19] but was observed to be an FM insulator with T_C of 72 K;[27,44,45] therefore, its reported multiferroic properties[29] need further verification because an FM structure does not produce ferroelectric polarization.[27] Up to now, only In_2NiMnO_6 ($r_{VIII}(In^{3+})$ = 0.92 Å) shows AFM behavior, suggesting that antiferromagnetism can only appear in R_2NiMnO_6 with R ions below a critical radius[33] from which it is natural to suspect that the ordered state in Sc_2NiMnO_6 ($r_{VIII}(Sc^{3+})$ = 0.870 Å) may also be AFM.

Figure 3 shows the temperature and magnetic field dependence of the specific heat capacity C_p of Sc_2NiMnO_6. Two large peaks are observed at T_1 = 35 K and T_2 = 17 K, corresponding to two phase transitions that are bulk in nature. A magnetic field has a negligible effect on the transition at T_1, whereas a moderate magnetic field reduces T_2 by approximately

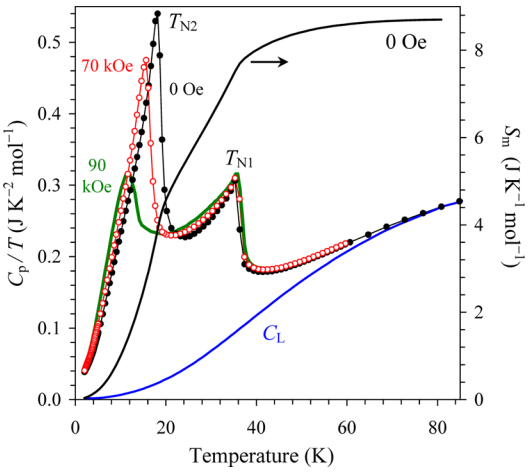

Figure 3. Heat capacity $C_p(T)$ of Sc_2NiMnO_6 in the form of C_p/T vs T between 2 and 84 K at various H. (The molecular weight is calculated for the ABO_3 composition.) The thin blue line shows the lattice contribution (from $ScRhO_3$). The right-hand axis gives the temperature dependence of magnetic entropy.

1 K/Tesla. The lattice contribution (C_L) to the total specific heat C_p was estimated by using the data of nonmagnetic $ScRhO_3$,[46] that is, $C_L = C_p(ScRhO_3)$ (Figure S4). The magnetic contribution (C_M) was thus obtained through $C_M(ScNi_{0.5}Mn_{0.5}O_3) = C_p(ScNi_{0.5}Mn_{0.5}O_3) - C_L$. The magnetic entropy was obtained using the thermodynamic relationship $S_m = \int(C_m/T)dT$. The entropy associated with the phase transitions is found to be about 17.4 J K^{-1} mol^{-1} (for Sc_2NiMnO_6), more than 84% of the expected value, 20.7 J K^{-1} mol^{-1}, suggesting most of the entropy is removed. Because T_1 and T_2 are close, it is very difficult to unambiguously estimate the entropy at each transition.

The temperature-dependent magnetic susceptibility (χ vs T) of Sc_2NiMnO_6 is presented in Figure 4 (top). ZFC and FC

DOI: 10.1021/acs.inorgchem.5b01195
Inorg. Chem. XXXX, XXX, XXX−XXX

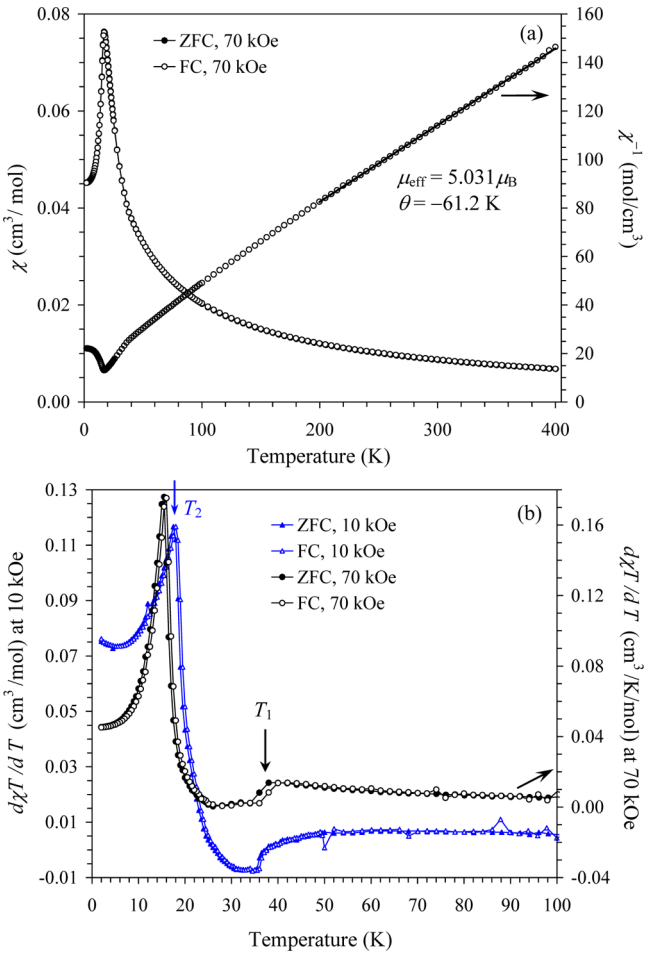

Figure 4. Top: Temperature dependence of χ for Sc_2NiMnO_6 at H = 70 kOe. The right-hand axis gives the reciprocal χ^{-1} with the Curie–Weiss fit (solid line). Bottom: Temperature dependence of χ in a form $d\chi T/dT$ vs T at 10 kOe (left-hand axis) and 70 kOe (right-hand axis).

curves are virtually indistinguishable, and a sharp peak is visible at T_2 = 17 K in both. A plot of χ^{-1} versus T was fit to a Curie–Weiss (CW) law, shown by the solid curve. A least-squares fit to the paramagnetic range between 200 and 400 K yielded θ_{CW} = −61.2(7) K and μ_{eff} = 5.031(5)μ_B/f.u. (f.u. is formula unit); these values were independent of the measuring field H. The negative θ_{CW} indicates dominant AFM interactions, consistent with the magnetic structure results presented later. The measured μ_{eff} is close to that of In_2NiMnO_6 (μ_{eff} = 4.891μ_B)[33] and to the expected value of 4.796 μ_B/f.u. for Sc_2NiMnO_6 with one Mn^{4+} (S = 3/2) and one Ni^{2+} (S = 1). Although no obvious anomalies appear at other temperatures, the reciprocal χ^{-1} versus T curve shows a kink at T_1 = 35 K, seen in Figure 4 (top), which can be more easily observed in the $d\chi T/dT$ versus T curves of Figure 4 (bottom). The linear M versus H dependence of the isothermal magnetization measured at 2 K (Figure S5) indicates that the ground state is a fully compensated antiferromagnet.

The magnetic nature of the two transitions was confirmed by Mössbauer spectroscopy of Sc_2NiMnO_6:0.5%^{57}Fe (Figure 5). Spectra above T_1 (at 300 and 45 K) consist of paramagnetic doublets, Fe1 and Fe2, with different isomer shifts (δ_{Fe1} = 0.35(1) and δ_{Fe2} = 0.42(1) mm/s, at 300 K) and quadrupole splittings (Δ_{Fe1} = 0.56(2) and Δ_{Fe2} = 1.38(1) mm/s). From our investigation of several $ScMO_3$ and $InMO_3$ perovskites with M = 3d transition metals,[47] we found that the Fe1 and Fe2 doublets originate from $^{57}Fe^{3+}$ cations located in the B and A sublattices of the perovskite structure, respectively. For Sc_2NiMnO_6:0.5%^{57}Fe, it means that a small amount of $^{57}Fe^{3+}$ cations is located at the Sc site. The Fe2 contribution (from the Sc sublattice) is not important for our discussion. Spectra at 25 K (between T_1 and T_2) have two hyperfine magnetic contributions: the first subspectrum, $Fe1_m$, is a well-defined six-line Zeeman sextet, and the second subspectrum, $Fe2_m$, has a continuous distribution of hyperfine magnetic field. The distribution of internal fields for $Fe2_m$ extends to zero (Figure 5d), indicating that some of the $^{57}Fe^{3+}$ ions are not subject to any static magnetic fields. The Mössbauer spectra between T_1 and T_2 suggest quite different magnetic environments of the $^{57}Fe^{3+}$ cations at the Mn and Ni sites, although a priori it cannot be determined which signal belongs to which site. On the basis of further considerations (see later text), we interpret the well-defined Zeeman sextet as originating from $^{57}Fe^{3+}$ cations located at the Mn site. Below T_2 (at 12 K), the distribution function for the $Fe2_m$ subspectrum changes from continuous to discrete, indicating the onset of long-range ordering in both sublattices.

The frequency-dependent dielectric constant of Sc_2NiMnO_6 is shown in Figures 6 and S8 as a function of temperature, $\varepsilon(T)$. The curves start to increase more rapidly on lowering temperature below T_1 until reaching a maximum at T_2, below which the $\varepsilon(T)$ curves drop rapidly. In contrast to the $\varepsilon(T)$ of compounds such as $LnMnO_3$ (Ln = Y and Ho–Lu),[48,49] no temperature hysteresis is visible during cooling and warming.

The $\varepsilon(T)$ curves in applied magnetic fields of up to 90 kOe at a fixed frequency of 46.4 kHz are shown in Figure 7a. The peak in $\varepsilon(T)$ is sensitive to H, shifting from ∼17 K at H = 0 to 12.5 K at H = 90 kOe in the same manner as the ordering temperature determined from the heat capacity. The MD ratio $\varepsilon_{MD}(H)$, defined as $\varepsilon_{MD} = [\varepsilon(H) - \varepsilon(0)]/\varepsilon(0) \times 100\%]$, is plotted in Figure 7b, and its behavior can be understood from the large sensitivity of T_2 to an applied field. Just above 18 K, $\varepsilon_{MD}(H)$ is negative owing to the suppression of the peak in ε at T_2, while below 18 K, $\varepsilon_{MD}(H)$ increases until T_2 is coincident with the temperature, after which $\varepsilon_{MD}(H)$ decreases rapidly.

We also attempted to measure the electric polarization as a function of temperature and found no evidence for any pyroelectric current, demonstrating that the dielectric anomaly is not due to a ferroelectric transition. The anomaly could be attributed to antiferroelectric behavior as is observed in some double-perovskites with the formula $Pb_2MM'O_6$ (M = Mg, Co, Ni, Zn, Sc, and Fe; M′ = Ti, Zr, Nb, Ta, and W)[50,51] because of an order–disorder transition of the local structure. There are also cases where antiferroelectric distortions arise from magnetoelastic coupling associated with a magnetic phase transition.[52]

The results of the crystal structure refinement against the neutron diffraction data (Figure 8, Table 2) are fully consistent with the synchrotron XRD results above. The opposite signs of the neutron scattering lengths b(Mn) and b(Ni) allow a robust determination of the degree of B-site ordering, which is found to be 100(4)%. New diffraction peaks appear in the phase below T_1 = 35 K, which we label AFM I. These peaks can be indexed with the propagation vector $\mathbf{k_1}$ = (1/2, 0, 1/2). Additional peaks appear below 17 K (AFM II) which can be indexed by the propagation vector $\mathbf{k_2}$ = (0, 1/2, 1/2), and these peaks coexist with the peaks belonging to $\mathbf{k_1}$ together forming a 2-$\mathbf{k}$ magnetic structure. Rietveld refinement of the diffraction

DOI: 10.1021/acs.inorgchem.5b01195
Inorg. Chem. XXXX, XXX, XXX–XXX

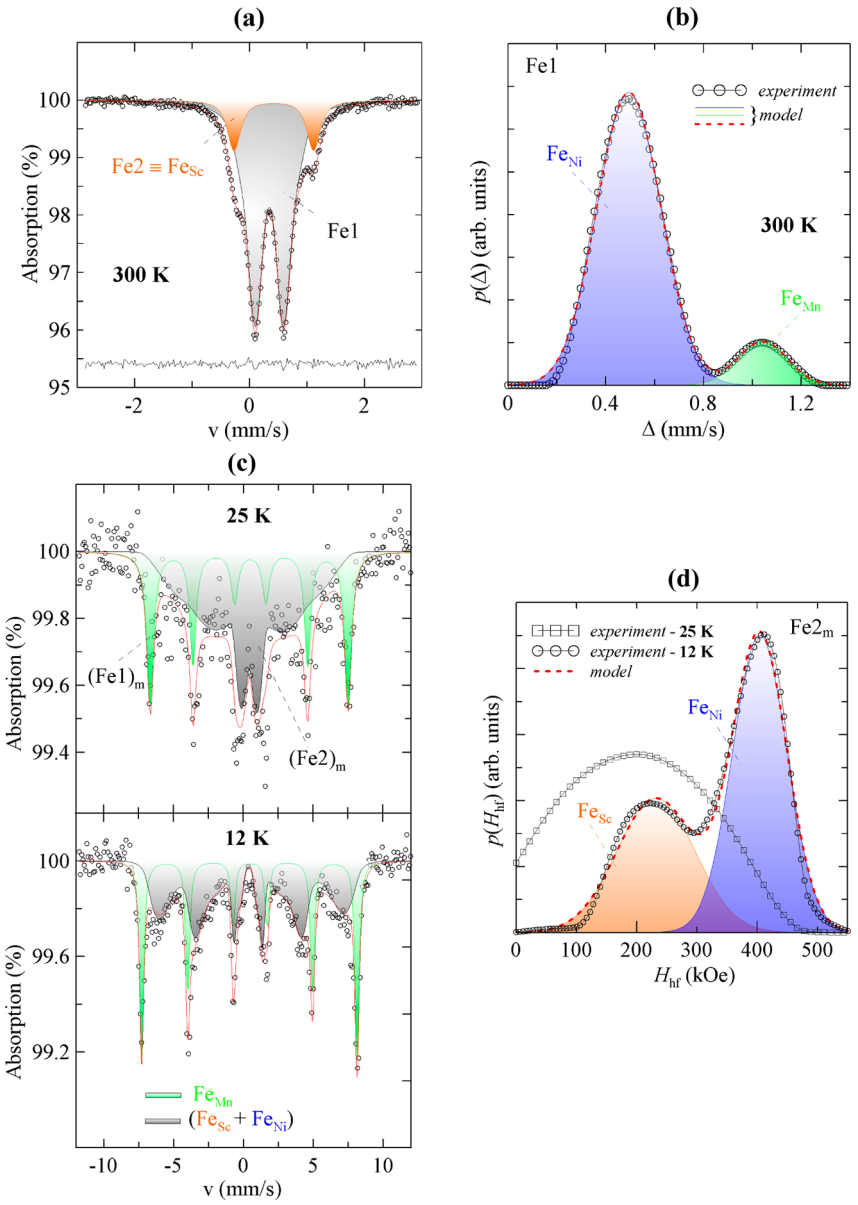

Figure 5. ^{57}Fe Mössbauer spectra of Sc_2NiMnO_6:0.5%^{57}Fe (experimental data are white symbols) at (a) 300 K and (c) 25 and 12 K and fitting results. (b) Distribution, $p(\Delta_{Fe1})$, of the quadrupole splitting, Δ_{Fe1}, for the Fe1 doublet on the panel a. (d) Distribution, $p(H_{hf})$, of hyperfine magnetic fields, H_{hf}, for the $Fe2_m$ subspectrum at 12 and 25 K from the panel c.

pattern was performed with the FullProf software,[53] and symmetry analysis was performed with both the Basireps and ISODISTORT packages.[54,55] The space group $P2_1/n$ has only one magnetic irreducible representation (irrep) associated with $\mathbf{k}_2$ = (0, 1/2, 1/2) which is the 1-D complex representation mD1−D2−.[56] There are four different magnetic irreps associated with $\mathbf{k}_1$ = (1/2, 0, 1/2) which are the 1-D irreps mY1+, mY2+, mY1−, and mY2−. The Y1± and Y2± type representations enforce a specific relation between the magnetic moments on the two equivalent Mn/Ni sites where either the x and z components of the magnetic moment change sign or only the y component changes sign. The mYn+ (mYn−) type representations, importantly, specify a magnetic order on only the Mn (Ni) sublattice, a consequence of the different behavior of these sites under the inversion operation. Energetically, it is difficult to understand why the two sublattices would not order coincidently unless the Ni−O−Mn superexchange was either highly frustrated or suppressed, in which case the system might naturally select a magnetic ordering wavevector which produces a vanishing molecular field at the site of the other transition-metal ion. A phase transition involving both the Ni and Mn irreps would remove the inversion center, reducing the space group symmetry to either $P2_1$ or Pn and allowing ferroelectricity. However, there is no measurable anomaly in the lattice parameters associated with AFM I (Figure S9), nor is there a substantial dielectric anomaly until T_2 (associated with the second phase, AFM II), both of which would be anticipated in the case of a ferroelectric phase transition. Therefore, the combined evidence from neutron diffraction and the dielectric response strongly suggests that the spins on the Mn and Ni sites order independently. Mössbauer measurements give a further support for this conclusion.

Given that the spins on the two transition-metal sublattices (Mn and Ni) order independently, it remains to identify which sublattice orders with which propagation vector, $\mathbf{k}_1$ or $\mathbf{k}_2$. This information cannot be determined from the diffraction data.

DOI: 10.1021/acs.inorgchem.5b01195
Inorg. Chem. XXXX, XXX, XXX−XXX

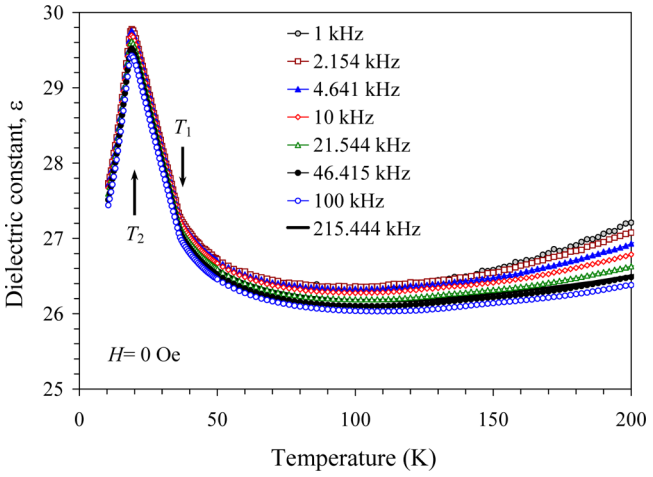

Figure 6. Temperature dependence of dielectric constant of Sc_2NiMnO_6 at various frequencies. The vertical arrows show the magnetic transition temperatures T_1 and T_2.

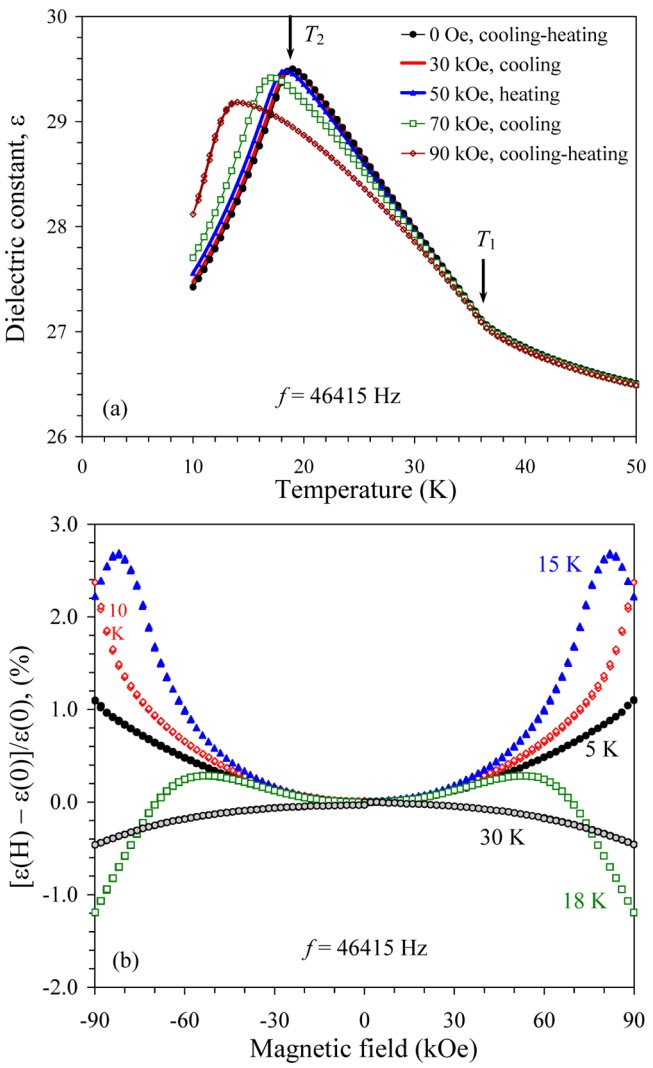

Figure 7. (a) Temperature dependence of dielectric constant at various magnetic fields of Sc_2NiMnO_6 at fixed frequency of f = 46 415 Hz. (b) The H dependence of ε_{MD} of Sc_2NiMnO_6 at various temperatures and fixed f = 46 415 Hz.

Instead, we have used a mean-field Heisenberg model to analyze the stability of the magnetic structures and have calculated the dominant Ni−O−O−Ni and Mn−O−O−Mn extended superexchange interactions using the CAESAR program[57] (see Figure S10). The $\mathbf{k_1}$ magnetic structure requires a dominant AFM interaction between equivalent sites separated by a distance a along the a axis, and the CAESAR calculations show that this condition applies to the Mn sublattice but not to the Ni sublattice. Hence, we infer that it is the Mn spins which order at T_1 = 35 K with propagation vector $\mathbf{k_1}$, and the Ni spins order at T_2 = 17 K with propagation vector $\mathbf{k_2}$.

To refine the details of the magnetic structures further, we first fitted the paramagnetic phase with data from banks 2 through 9 of the WISH instrument in order to accurately determine the instrument and structural parameters. Below T_1, we fixed the instrumental parameters and fitted only the background, atomic coordinates, lattice parameters, isotropic thermal displacements, absorption, and scale. We fitted the magnetic data only from banks 2 and 9, which contain the most information on the magnetic structure as they capture the largest d-spacings, and from these two banks, we subtract the high-temperature data to obtain only the magnetic peaks. For the AFM I phase, we allowed the components of the Mn moment (M_a, M_b, M_c) to freely refine, and we obtained excellent agreement with the data with the parameters found in Table 2. For the AFM II phase, we refined a magnetic moment on the Ni site in addition to that on the Mn site. For the fit to converge, it was necessary to fix the M_b-component of the Ni magnetic moment to be zero. The magnetic peak widths for this phase are broader, indicating a shorter correlation length for the Ni sublattice and necessitating the free refinement of the associated peak-width parameters. The results of the refinement at 1.5 K are tabulated in Table 2, and the refined structures are shown in Figure 9. The combination of two $\mathbf{k}$-vectors and two active irreps below T_2 is compatible with a magnetostrictive antiferroelectric effect which would be capable of producing the observed dielectric anomaly.

The two AFM ordered states detailed above are both unusual for a double perovskite lattice with 3d ions on the B-sites. For example, the Ni−O−Mn nearest-neighbor exchange is expected to be FM according to the G-K rules, and deviations from this are commonly a result of coupling between a 3d cation and either a 4d or 5d cation such as in Sr_2CoOsO_6.[13] After In_2NiMnO_6, Sc_2NiMnO_6 is only the second B-site-ordered double perovskite in the $R_2BB'O_6$ family, where both B and B′ are 3d metals, to show AFM order. This can be partially understood from results on the R_2NiMnO_6 series, where the increased octahedral tilting associated with decreasing A-site cation radius is a key ingredient in suppressing the FM nearest neighbor (FM-NN) exchange (Figure S3). However, the ordering vector $\mathbf{k_1}$ = (1/2, 0, 1/2) (which has not, to our knowledge, been reported in any other double perovskites containing 3d ions at the B and B′ sites) is particularly notable here as it produces no molecular field at the sites of the Ni atoms, alleviating the competition between FM-NN and AFM-NNN superexchanges. Moreover, the occurrence of two separate magnetic phase transitions, apparently associated with the independent ordering of the two 3d ions, appears to be unique among all known oxides and is surprising given the near ubiquity of ferromagnetism in similar materials driven by FM Ni−O−Mn superexchange.

From the results obtained for Sc_2NiMnO_6, a schematic magnetic phase diagram of the R_2NiMnO_6 family (R = Sc, In,

DOI: 10.1021/acs.inorgchem.5b01195
Inorg. Chem. XXXX, XXX, XXX−XXX

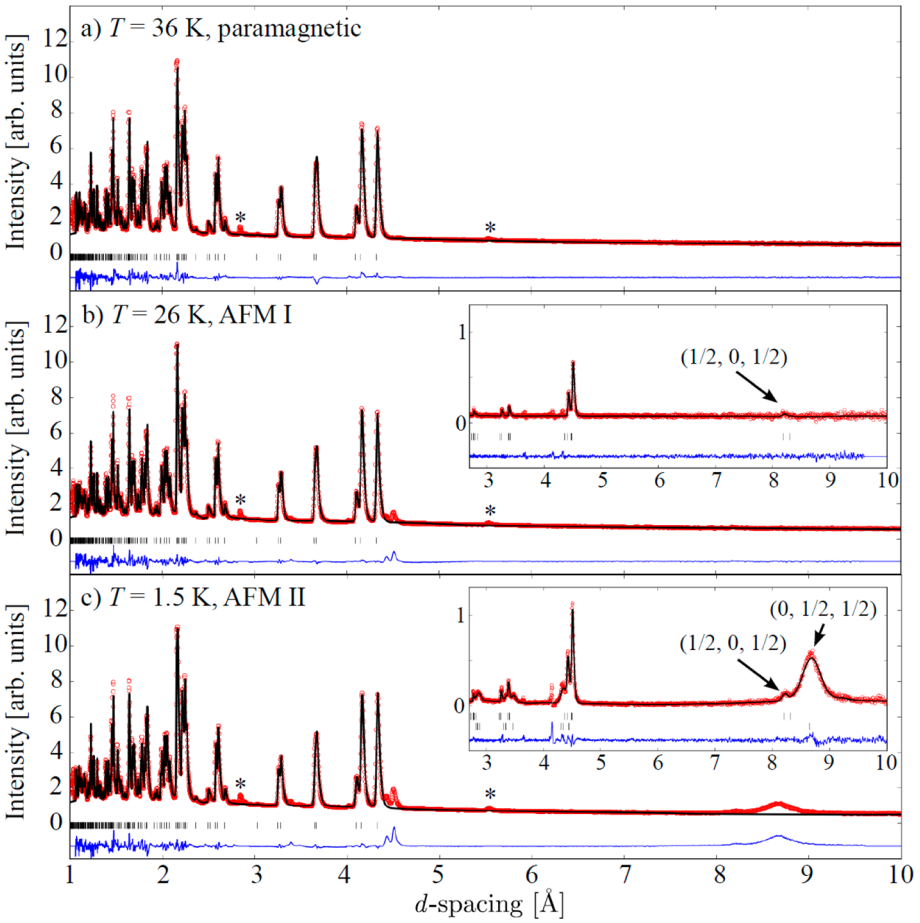

Figure 8. Neutron powder patterns merged from banks 2 and 9 on WISH recorded in (a) the paramagnetic phase, (b) AFM I, and (c) AFM II. Observed (red), calculated (black), and difference (blue) profiles. Asterisks mark a small amount (<5%) of Sc_2O_3 impurity. The magnetic-only diffraction patterns, with the nuclear peaks subtracted, are shown in the insets. The refinements in the main panels include the nuclear contributions only. The small tick marks denote simulated peak positions for the corresponding contributions.

Table 2. Refined Values of the Crystal and Magnetic Structures from the 2nd and 9th Banks of WISH at 1.5 K

site	x	y	z	B (Å^2)
Mn	0.5	0	0.5	0.89(99)
Ni	0.5	0	0	0.29(67)
Sc	0.973(1)	0.077(1)	0.254(1)	2.56(61)
O1	0.366(2)	0.938(3)	0.258(2)	1.09(69)
O2	0.192(3)	0.184(3)	0.563(2)	1.07(76)
O3	0.674(3)	0.300 (3)	0.426(2)	0.86(71)
site	M_a	M_b	M_c	k-vector
Mn	1.17(18)	−0.01(1)	1.19(23)	(1/2,0,1/2)
Ni	−1.03(42)	0 (−)	−1.09(27)	(0,1/2,1/2)

Space group $P2_1/n$, lattice constants a = 4.99086(5) Å, b = 5.35269(6) Å, c = 7.34122(8) Å, β = 90.869(1)°. Final R values for the 1.5 K pattern were R_{Bragg} = 4.6%, R_{mag} (Mn) = 3.13%, and R_{mag} (Ni) = 2.37%.

Y, and rare-earth elements) with the ordered $P2_1/n$ structure can be constructed (Figure 10). This phase diagram resembles, to some extent, a magnetic phase diagram of $LnMnO_3$, where complex noncollinear magnetic structures are sandwiched between basically collinear magnetic structures of the *A*-type (with a small spin canting) and *E*-type.[58] In R_2NiMnO_6, a complex noncollinear magnetic structure found in In_2NiMnO_6[35] is sandwiched between FM (with a small canting)[30] and AFM collinear magnetic structures.

CONCLUSION

Sc_2NiMnO_6 has been successfully synthesized by a high-pressure method and has been found to have the room-temperature space group $P2_1/n$. Below T_1 = 35 K, the material orders antiferromagnetically with a propagation vector $\mathbf{k_1}$ = (1/2, 0, 1/2), while below T_2 = 17 K an additional AFM component with a propagation vector of $\mathbf{k_2}$ = (0, 1/2, 1/2) appears. We have presented a model which describes a unique scenario whereby the Mn ions order at T_1 with $\mathbf{k_1}$, and the Ni ions order at T_2 with $\mathbf{k_2}$. This would imply that nearest-neighbor superexchange between Ni and Mn is heavily suppressed compared to the next-nearest-neighbor Ni−Ni and Mn−Mn extended superexchanges. The dielectric anomaly onsets only in response to the second magnetic ordering, that is, when both sublattices are magnetically ordered, which could be explained by the onset of antiferroelectricity in response to an intersublattice magnetostriction. The magnetic field dependence of the dielectric anomaly is yet to be fully understood. These results suggest that small A-site cations in B-site-ordered double perovskites of magnetic 3d ions represent an interesting playground for the exploration of magnetoelectric phenomena.

DOI: 10.1021/acs.inorgchem.5b01195
Inorg. Chem. XXXX, XXX, XXX−XXX

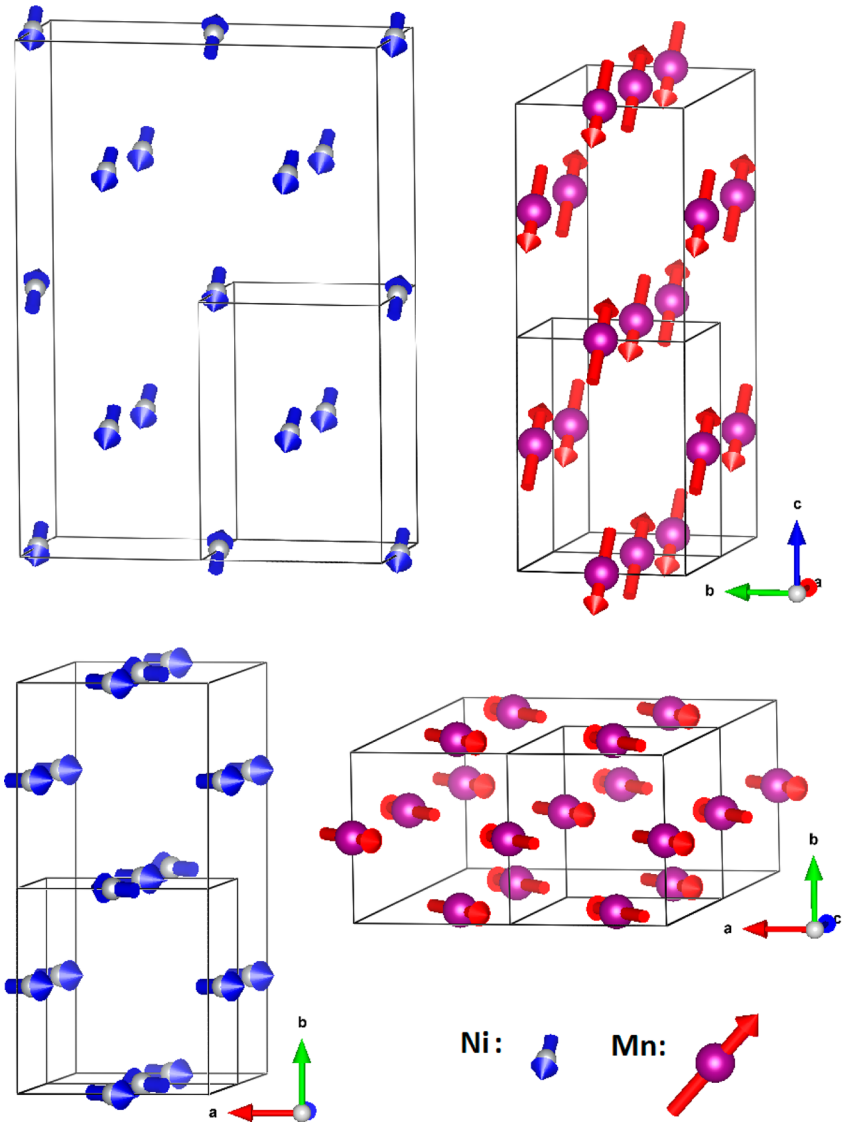

Figure 9. Refined magnetic structure (in phase AFM II), with the blue arrows as the Ni^{2+} moments and the Mn^{4+} moments in red. The moments lie primarily in the *ac*-plane at an angle of almost 45° to the *a*-axis. A nuclear cell is $^1/_8$ of the total magnetic cell. The figure is produced using VESTA.[39]

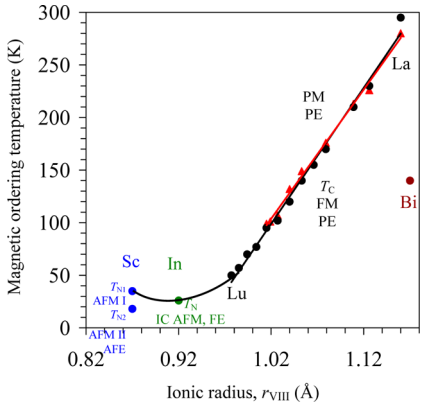

Figure 10. Magnetic phase diagram of the R_2NiMnO_6 family (R = Sc, In, Y, and rare-earth elements) with the ordered $P2_1/n$ structure.[33,35,45] PM, paramagnetic; FM, ferromagnetic; AFM, (collinear) antiferromagnetic; IC AFM, incommensurate antiferromagnetic; T_N, the AFM Neel temperature; T_C, the FM Curie temperature; PE, paraelectric; FE, ferroelectric; AFE, antiferroelectric. T_C of Bi_2NiMnO_6, crystallizing in a different structure,[15] is shown for comparison.

■ ASSOCIATED CONTENT

Supporting Information

The Supporting Information is available free of charge on the ACS Publications website at DOI: 10.1021/acs.inorgchem.5b01195.

Partial refined crystal structure details, isothermal magnetizations, detailed discussion of the Mössbauer spectra, and the details of specific heat and magnetic results and the mean-field analysis and CAESAR calculation (PDF)

■ AUTHOR INFORMATION

Corresponding Authors

*E-mail: Yangfeng.Guo@physics.ox.ac.uk.
*E-mail: Alexei.Belik@nims.go.jp.

Author Contributions

W. Yi and A. J. Princep contributed equally to this work. All authors have given approval to the final version.

DOI: 10.1021/acs.inorgchem.5b01195
Inorg. Chem. XXXX, XXX, XXX−XXX

Funding

This research was supported in part by the World Premier International Research Center Initiative (WPI Initiative, MEXT, Japan), the Japan Society for the Promotion of Science (JSPS) through its "Funding Program for World-Leading Innovative R&D on Science and Technology (FIRST Program)", the Grants in-Aid for Scientific Research (22246083) from JSPS, Japan, and the UK Engineering and Physical Sciences Research Council (grants EP/J012912/1 and EP/J017124/1).

Notes

The authors declare no competing financial interest.

■ ACKNOWLEDGMENTS

The authors would like to thank the staff of BL15XU and SPring-8 for their help with the use of the beamline. The synchrotron radiation experiments were performed at the SPring-8 with the approval of the Japan Synchrotron Radiation Research Institute (Proposal Numbers: 2011B4512 and 2012A4507). We thank Mr. K. Kosuda of NIMS for performing the EPMA measurements.

■ REFERENCES

(1) Mostovoy, M.; Scaramucci, A.; Spaldin, N. A.; Delaney, K. T. *Phys. Rev. Lett.* **2010**, *105*, 087202.
(2) Kitagawa, Y.; Hiraoka, Y.; Honda, T.; Ishikura, T.; Nakamura, H.; Kimura, T. *Nat. Mater.* **2010**, *9*, 797−802.
(3) Tackett, R.; Lawes, G.; Melot, B. C.; Grossman, M.; Toberer, E. S.; Seshadri, R. *Phys. Rev. B: Condens. Matter Mater. Phys.* **2007**, *76*, 024409.
(4) Lawes, G.; Ramirez, A. P.; Varma, C. M.; Subramanian, M. A. *Phys. Rev. Lett.* **2003**, *91*, 257208.
(5) Kimura, T.; Goto, T.; Ishizaka, H.; Arima, T.; Tokura, Y. *Nature* **2004**, *426*, 55−58.
(6) Cheong, S. W.; Mostovoy, M. *Nat. Mater.* **2007**, *6*, 13−20.
(7) Saito, M.; Higashinaka, R.; Maeno, Y. *Phys. Rev. B: Condens. Matter Mater. Phys.* **2005**, *72*, 144422.
(8) Katsufuji, T.; Takagi, T. *Phys. Rev. B: Condens. Matter Mater. Phys.* **2004**, *69*, 064422.
(9) Hur, N.; Park, S.; Guha, S.; Borissov, A.; Kiryukhin, V.; Cheong, S.-W. *Appl. Phys. Lett.* **2005**, *87*, 042901.
(10) Vasala, S.; Karppinen, M. *Prog. Solid State Chem.* **2015**, *43*, 1−36.
(11) Dass, R. I.; Yan, J. Q.; Goodenough, J. B. *Phys. Rev. B: Condens. Matter Mater. Phys.* **2003**, *68*, 064415.
(12) Paul, A. K.; Reehuis, M.; Ksenofontov, V.; Yan, B.; Hoser, A.; Többens, D. M.; Abdala, P. M.; Adler, P.; Jansen, M.; Felser, C. *Phys. Rev. Lett.* **2013**, *111*, 167205.
(13) Morrow, R.; Mishra, R.; Restrepo, O. D.; Ball, M. R.; Windl, W.; Wurmehl, S.; Stockert, U.; Büchner, B.; Woodward, P. M. *J. Am. Chem. Soc.* **2013**, *135*, 18824−18830.
(14) (a) Feng, H. L.; Arai, M.; Matsushita, Y.; Tsujimoto, Y.; Guo, Y. F.; Sathish, C. I.; Wang, X.; Yuan, Y. H.; Tanaka, M.; Yamaura, K. *J. Am. Chem. Soc.* **2014**, *136*, 3326−3329. (b) Feng, H. L.; Arai, M.; Matsushita, Y.; Tsujimoto, Y.; Yuan, Y. H.; Sathish, C. I.; He, J. F.; Tanaka, M.; Yamaura, K. *J. Solid State Chem.* **2014**, *217*, 9−15.
(15) Azuma, M.; Takata, K.; Saito, T.; Ishiwata, S.; Shimakawa, Y.; Takano, M. *J. Am. Chem. Soc.* **2005**, *127*, 8889−8892.
(16) Yáñez-Vilar, S.; Mun, E. D.; Zapf, V. S.; Ueland, B. G.; Thompson, J. D.; Singleton, J.; Sánchez-Andújar, M.; Mira, J.; Biskup, N.; Señarís-Rodríguez, M. A.; Batista, C. D. *Phys. Rev. B: Condens. Matter Mater. Phys.* **2011**, *84*, 134427.
(17) Sharma, G.; Saha, J.; Kaushik, S. D.; Siruguri, V.; Patnaik, S. *Appl. Phys. Lett.* **2013**, *103*, 012903.
(18) Battle, P. D.; Gibb, T. C.; Jones, C. W.; Stude, F. *J. Solid State Chem.* **1989**, *78*, 281−293.
(19) Kumar, S.; Giovannetti, G.; van den Brink, J.; Picozzi, S. *Phys. Rev. B: Condens. Matter Mater. Phys.* **2010**, *82*, 134429.
(20) Singh, M. P.; Truong, K. D.; Jandl, S.; Fournier, P. *J. Appl. Phys.* **2010**, *107*, 09D917.
(21) Bhattacharjee, S.; Eriksson, O.; Sanyal, B. *J. Phys.: Condens. Matter* **2012**, *24*, 295901.
(22) Goodenough, J. B. *Phys. Rev.* **1955**, *100*, 564−573.
(23) Kanamori, J. *J. Phys. Chem. Solids* **1959**, *10*, 87−98.
(24) Manna, K.; Joshi, R. S.; Elizbeth, S.; Anil Kumar, P. S. *Appl. Phys. Lett.* **2014**, *104*, 202905.
(25) Lee, N.; Choi, H. Y.; Jo, Y. J.; Seo, M. S.; Park, S. Y.; Choi, Y. J. *Appl. Phys. Lett.* **2014**, *104*, 112907.
(26) (a) Rogado, N. S.; Li, J.; Sleight, A. W.; Subramanian, M. A. *Adv. Mater.* **2005**, *17*, 2225−2227. (b) Choudhury, D.; Mandal, P.; Mathieu, R.; Hazarika, A.; Rajan, S.; Sundaresan, A.; Waghmare, U. V.; Knut, R.; Karis, O.; Nordblad, P.; Sarma, D. D. *Phys. Rev. Lett.* **2012**, *108*, 127201.
(27) Kakarla, D. C.; Jyothinagaram, K. M.; Das, A. K.; Adyam, V. *J. Am. Ceram. Soc.* **2014**, *97*, 2858−2866.
(28) Zhou, H. Y.; Zhao, H. J.; Zhang, W. Q.; Chen, X. M. *Appl. Phys. Lett.* **2015**, *106*, 152901.
(29) (a) Zhang, C. Y.; Zhang, T. S.; Ge, L.; Wang, S.; Yuan, H. M.; Feng, S. H. *RSC Adv.* **2014**, *4*, 50969−50974. (b) Su, J.; Yang, Z. Z.; Lu, X. M.; Zhang, J. T.; Gu, L.; Lu, C. J.; Li, Q. C.; Liu, J.-M.; Zhu, J. S. *ACS Appl. Mater. Interfaces* **2015**, *7*, 13260−13265.
(30) Manna, K.; Bera, A. K.; Jain, M.; Elizabeth, S.; Yusuf, S. M.; Anil Kumar, P. S. *Phys. Rev. B: Condens. Matter Mater. Phys.* **2015**, *91*, 224420.
(31) Katari, V.; Achary, S. N.; Deshpande, S. K.; Babu, P. D.; Sinha, A. K.; Salunke, H. G.; Gupta, N.; Tyagi, A. K. *J. Phys. Chem. C* **2014**, *118*, 17900−17913.
(32) Chandrasekhar, K. Devi.; Das, A. K.; Mitra, C.; Venimadhav, A. *J. Phys.: Condens. Matter* **2012**, *24*, 495901.
(33) Yi, W.; Liang, Q.; Matsushita, Y.; Tanaka, M.; Belik, A. A. *Inorg. Chem.* **2013**, *52*, 14108−14115.
(34) Belik, A. A.; Yi, W. *J. Phys.: Condens. Matter* **2014**, *26*, 163201.
(35) Terada, N.; Khalyavin, D. D.; Manuel, P.; Yi, W.; Suzuki, H. S.; Tsujii, N.; Imanaka, Y.; Belik, A. A. *Phys. Rev. B: Condens. Matter Mater. Phys.* **2015**, *91*, 104413.
(36) Thomas, C. I.; Suchomel, M. R.; Duong, G. V.; Fogg, A. M.; Claridge, J. B.; Rosseinsky, M. J. *Philos. Trans. R. Soc., A* **2014**, *372*, 20130012.
(37) (a) Tanaka, M.; Katsuya, Y.; Yamamoto, A. *Rev. Sci. Instrum.* **2008**, *79*, 075106. (b) Tanaka, M.; Katsuya, Y.; Matsushita, Y.; Sakata, O. *J. Ceram. Soc. Jpn.* **2013**, *121*, 287−290.
(38) Izumi, F.; Ikeda, T. *Mater. Sci. Forum* **2000**, *321*−*324*, 198−205.
(39) Momma, K.; Izumi, F. *J. Appl. Crystallogr.* **2008**, *41*, 653−658.
(40) Chapon, L. C.; Manuel, P.; Radaelli, P. G.; Benson, C.; Perrott, L.; Ansell, S.; Rhodes, N. J.; Raspino, D.; Duxbury, D.; Spill, E.; Norris, J. *Neutron News* **2011**, *22*, 22−25.
(41) Werner, P. E.; Eriksson, L.; Westdahl, M. *J. Appl. Crystallogr.* **1985**, *18*, 367−370.
(42) Brese, N. E.; O'Keeffe, M. *Acta Crystallogr., Sect. B: Struct. Sci.* **1991**, *47*, 192−197.
(43) Glazer, A. M. *Acta Crystallogr., Sect. B: Struct. Crystallogr. Cryst. Chem.* **1972**, *B28*, 3384−3392.
(44) Zhao, H. J.; Liu, X. Q.; Chen, X. M.; Bellaiche, L. *Phys. Rev. B: Condens. Matter Mater. Phys.* **2014**, *90*, 195147.
(45) (a) Asai, K.; Fujiyoshi, K.; Nishimori, N.; Satoh, Y.; Kobayashi, Y.; Mizoguchi, M. *J. Phys. Soc. Jpn.* **1998**, *67*, 4218−4228. (b) Booth, R. J.; Fillman, R.; Whitaker, H.; Nag, A.; Tiwari, R. M.; Ramanujachary, K. V.; Gopalakrishnan, J.; Lofland, S. E. *Mater. Res. Bull.* **2009**, *44*, 1559−1564.
(46) Belik, A. A.; Matsushita, M.; Tanaka, M.; Takayama-Muromachi, E. *Inorg. Chem.* **2013**, *52*, 12005−12011.
(47) Yi, W.; Presniakov, I. A.; Sobolev, A. V.; Glazkova, Y. S.; Matsushita, Y.; Tanaka, M.; Kosuda, K.; Tsujimoto, Y.; Yamaura, K.; Belik, A. A. *Sci. Technol. Adv. Mater.* **2015**, *16*, 024801.

DOI: 10.1021/acs.inorgchem.5b01195
Inorg. Chem. XXXX, XXX, XXX−XXX

(48) Pomjakushin, V. Yu.; Kenzelmann, M.; Doenni, A.; Harris, A. B.; Nakajima, T.; Mitsuda, S.; Tachibana, M.; Keller, L.; Mesot, J.; Kitazawa, H.; Takayama-Muromachi, E. *New J. Phys.* **2009**, *11*, 043019.
(49) Wang, L. J.; Chai, Y. S.; Feng, S. M.; Zhu, J. L.; Manivannan, N.; Jin, C. Q.; Gong, Z. Z.; Wang, X. H.; Li, L. T. *J. Appl. Phys.* **2012**, *111*, 114103.
(50) Gagulin, V. V.; Fadeeva, N. V.; Belous, A. G.; Sevastianova, L. A.; Titov, A. V.; Pltnikova, M. V.; Mitrofanov, K. P.; Zubova, E. V.; Solovev, S. P.; Venevtsev, Yu. N. *Phys. Status. Solidi a* **1977**, *44*, 247−256.
(51) Subêas, G.; Blasco, J.; García, J.; Herrero-Martín, J.; Sánchez, M. C. *J. Phys.: Condens. Matter* **2009**, *21*, 075903.
(52) Varignon, J.; Bristowe, N. C.; Bousquet, E.; Ghosez, P. 2014, aeXiv:1409.8422v1 [cond-mat.mtrl-sci].
(53) Wiles, D. B.; Young, R. A. *J. Appl. Crystallogr.* **1981**, *14*, 149; **1982**, *15*, 430−438.
(54) Rodríguez-Carvajal, J. *Phys. B* **1993**, *192*, 55−69.
(55) Campbell, B. J.; Stokes, H. T.; Tanner, D. E.; Hatch, D. M. *J. Appl. Crystallogr.* **2006**, *39*, 607−614.
(56) Miller, S. C.; Love, W. F. *Tables of Irreducible Representations of Space Groups and Co-Representations of Magnetic Space Groups*; Pruett: Boulder, U.S., 1967.
(57) Ren, J.; Liang, W.; Whangbo, M.-H. *CAESAR: crystal and electronic structure analyzer*; 1998. For details, see: http://www.PrimeC.com/.
(58) Tachibana, M.; Shimoyama, T.; Kawaji, H.; Atake, T.; Takayama-Muromachi, E. *Phys. Rev. B: Condens. Matter Mater. Phys.* **2007**, *75*, 144425.

DOI: 10.1021/acs.inorgchem.5b01195
Inorg. Chem. XXXX, XXX, XXX−XXX